CHAPTER 3

CLUMPY DISK EVOLUTION AND BCD MASS ASSEMBLY

3.1 Motivation

Unlike regular disk galaxies in the Local Universe, the high redshift galaxies during the *Cosmic Noon* (z~2) are clumpy and irregular which accounts for a considerable fraction of UV photons due to intense star formation [23, 71, 255–258, 372, 373]. The clumps are considerably larger (~1 kpc scales)[71, 255, 256, 258] than the star-forming regions seen in the nearby galaxies. It is important to note that giant star-forming clumps are quite common in galaxies with $M_* < 10^{9.8}$ $M_\odot$ [374] and that clumps residing in galaxy outskirts are forming stars at a higher rate than those in the inner regions[375]. In fact, a recent study by Mehta et al. 2023[376] finds that clumpy galaxies having stellar masses $< 10^{9.5}$ $M_\odot$ exhibit a more bursty star-formation history. The study also finds that there is an increase in the contribution from bursty star formation at larger distances from the galactic centre[376]. The evolution of clumpiness is also evident over cosmic time; with high redshift galaxies having a higher clump fraction[374, 375, 377] as compared to a scarcity of such clumps in the nearby Universe[378–380]. Studies of high redshift galaxies suggest that continuous infall of cold gas from the environment sustains such clumpy star formation[10, 243, 381–383]. At the same time, such clumps can migrate to the central regions thereby leading to bulge formation[22–25, 258]. In fact, such a picture is also indicated for BCDs in the nearby Universe[26] which in turn supports the centrally concentrated star formation. In this chapter, we focus on the young and outer star-forming clumps in the XUV disks of intermediate-z BCDs and their evolution.

3.2   Data analysis

From the *UVIT* imaging data, we could directly see FUV clumps in the BCD outskirts (Figure 3.1 and 3.2). The inner optical disk of the BCDs were also clumpy from visual inspection. We describe the methods to quantitatively extract these clumps as follows.

3.2.1   Clumps detection and stellar mass estimates

SExtractor parameters	
DETECT MINAREA	5
DETECT THRESH	**1.5**, 2, 2.5
FILTER NAME	**gauss 1.5 3x3.conv**, gauss 2.0 3x3.conv
DEBLEND NTHRESH	64
DEBLEND MINCONT	1×10^{-6}
CLEAN PARAM	10
BACK TYPE	MANUAL (locally obtained background as described above)

Noise Chisel parameters			
Detection		Segmentation	
erode	1	tilesize	40,40
erodengb	8	minskyfrac	0.1
tilesize	40 ,40	kernel	2 pixel fwhm
interpnumngb	4	interpnumngb	4
minskyfrac	0.1	snquant	0.4
meanmedqdiff	0.05	gthresh	1
detgrowquant	0.9	snminarea	4
noerodequant	0.9	objbordersn	1.0
dthresh	0.1		
snminarea	3		
sigmaclip	3,50		
qthresh	0.8		
snthresh	3.0		

Table 3.1: **Automated clump detection parameters.** The configuration for *SExtractor* and Noise Chisel used to detect the 'clumps'. A detection threshold of 1.5σ and gauss 1.5 pixel fwhm filter (boldface) has been used in our final calculations.

We identify young star-forming structures in the BCDs using a threefold approach. For this, we run *SExtractor*[21] and Noise Chisel[314] on the FUV cutouts of the BCDs, to detect and identify sources. We present the configurations of the tools in Table 3.1. In a few cases, both tools succeed in detecting but fail to deblend the faint structural irregularities in the outer parts. We

apply a visual approach in those cases. Here, we place elliptical apertures of sizes similar to the FUV PSF on these '*non-deblended*' structures. We estimate the S/N of the detections using the segmentation maps in both the cases of *SExtractor* (solid yellow contours in Figures 3.1 and 3.2), and Noise Chisel (marked by magenta dashed contours in Figures 3.1 and 3.2). We also estimate S/N in Kron-like apertures for those clumps identified using *SExtractor* (Table 3.3). For the visually identified sources, we estimate the S/N within fixed elliptical apertures (marked by red ellipses in Fig. 3.1 and 3.2. For all the identified sources, we consider only those having a S/N≥3 (or > 5σ above the background) for further analysis. Only those in the XUV region that do not have any *HST* counterpart are referred to as 'clumps' and considered to be part of the host BCD. We follow this definition of clumps throughout the text.

We convert the measured FUV fluxes of the clumps into SFRs[30] as follows:

$$SFR \ (M_\odot \ yr^{-1}) = 1.4 \ \times \ 10^{-28} \ L_\nu \ (ergs \ s^{-1} \ Hz^{-1}) \qquad (3.1)$$

Their stellar masses (see Table 3.3) are estimated assuming a constant SFR for 100 Myrs i.e. multiplying the SFR by a factor of 10^6. All clump stellar masses discussed in this chapter are FUV flux-derived unless specified. These masses are used for further calculations in the next section. All the stellar masses derived from FUV fluxes have been corrected for Galactic extinction as well as internal dust extinction with the help of the UV-slope (β). We obtain β by fitting a straight line within 1268Å - 2580Å , in λ vs F_λ space, to the intrinsic Spectral Energy Distribution (SED) models with FAST [315]. The colour excess E(B-V) is then obtained as[384]

$$E(B - V) = \frac{1}{4.684}[\beta + 2.616] \qquad (3.2)$$

3.2.2 In-spiral timescale due to dynamical friction

The timescale for in-plane accretion or in-spiral timescale, $T_{inspiral}$ of a clump can be determined by integrating the following equation for the rate of change
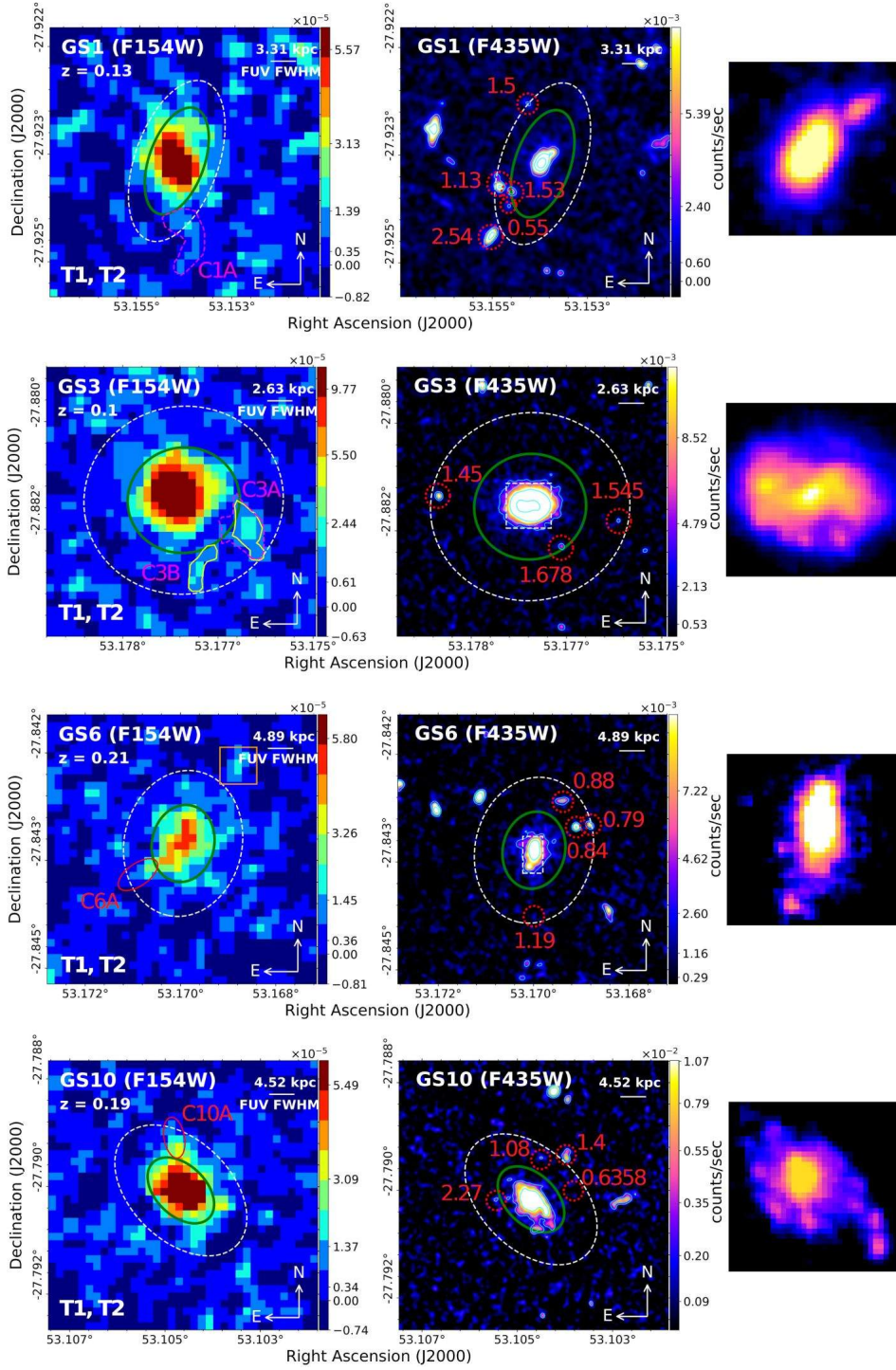
Figure 3.1: **Outer FUV clumps in the BCD sample.** In the first column are the FUV images of the BCDs and other two columns show the false colour HST-F435W band images. The identified clumps in the FUV do not have any HST counterpart as evident from the adjacent HST images in the second column. The solid yellow (and magenta dashed) contours mark those detected using *SExtractor* (and *Noise Chisel*). The red ellipses in UVIT images mark those identified manually. There are those marked in orange boxes outside the FUV extents which also do not have HST counterpart but we cannot confirm if they are associated with the galaxy and hence avoid them in our analysis. The third column shows the optical clumpy morphology in the inner regions of the BCDs. The cutouts in first two columns are of sizes 15"x15" whereas those in the third column are 2"x2" about the galaxy centers.
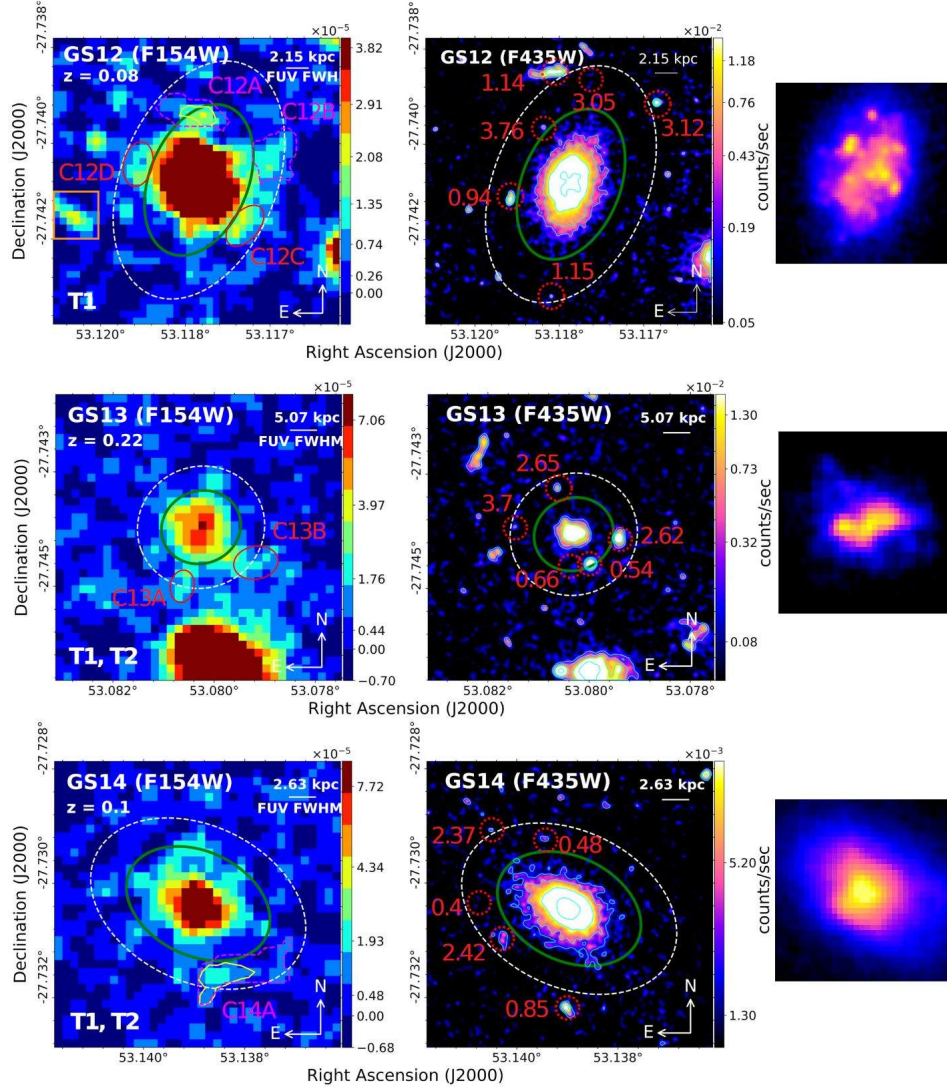
Figure 3.2: **Outer FUV clumps in the BCD sample**. Same as Figure 3.1. The cutout sizes for GS12 are 18"x18" and 4"x4" in the first two columns and third column respectively.

of orbital angular momentum:

$$d\vec{L}_z/dt = \vec{r} \times \vec{F}_{df} \qquad (3.3)$$

Here $\vec{F}_{df}$ refers to Chandrasekhar's instantaneous dynamical friction force[385, 386] acting on an orbiting clump of mass M_c due to the surrounding dark matter halo and is given by the following equation:

$$\vec{F}_{df} = -\frac{4\pi \ln \Lambda G^2 M_c^2 \rho}{V^2} \left(\text{erf} \left[X \right] - \frac{2X}{\pi^{1/2}} e^{-X^2} \right) \hat{V} = -\frac{4\pi \ln \Lambda G^2 M_c^2 \rho \xi}{V^2} \hat{V}; \quad (3.4)$$

where V is the clump orbital speed, $\hat{V}$ is the unit vector along the velocity direction, $X = V/(2^{1/2}\sigma)$ for halo 3D velocity dispersion σ with a Maxwellian distribution function, ρ is the halo density and ξ is the quantity in parentheses. The ξ term increases from 0 to 1 as X increases. The Coulomb factor $\ln \Lambda$ can be written as

$$\ln \Lambda = \ln \left(\frac{R_{gal}}{R_{min}} \right) \sim \ln \left(\frac{M_{dyn}}{M_c} \right) \sim \ln \left(\alpha \frac{M_*}{M_c} \right), \tag{3.5}$$

where R_{gal} is the size of the galaxy and $R_{\text{min}} \simeq GM_{\text{c}}/V^2$ is the strong encounter radius. Here α is a factor to convert the stellar mass (M_*) to dynamical mass (M_{dyn}). We assume $\alpha = 2.7$ for all BCDs as in the local BCD, NGC 4861[26].

We assume the dark matter halo to be pseudo-isothermal[386] with a core radius R_c and associated asymptotic rotation speed $V_0 = \sqrt{2}\sigma$. The potential for the DM halo is given by Binney's logarithmic spherical potential [386]:

$$\Phi_L(r) = \frac{V_0^2}{2} \ln[R_c^2 + r^2], \tag{3.6}$$

We use Poisson equation in spherical polar coordinate system to calculate density profile of the DM halo and it is given by the following equation:

$$\rho(r) = \frac{V_0^2}{4\pi G} \frac{(3R_c^2 + r^2)}{(R_c^2 + r^2)^2} \tag{3.7}$$

The above density profile is employed in the dynamical friction force calculation (in equation 3.4). While the clumps in-spiral, both the instantaneous velocity and radius changes with time but we assume the clump mass to remain intact. Considering this fact and substituting the dynamical friction force in equation 3.4, we can formally compute the in-spiral time as:

$$T_{inspiral} = \int_{R_{out}}^{R_{in}} \frac{V_0}{GM_c \ln \Lambda \xi} \frac{2R_c^2 + r^2}{3R_c^2 + r^2} \frac{r^2 dr}{\sqrt{R_c^2 + r^2}} \tag{3.8}$$

In the above equation, R_{out} and R_{in} refer to the clump outer and inner positions respectively. In the following we simplify the integral in terms of

dimensionless parameters; assuming the core radius, $R_c = pR_d$, where p is a constant number and R_d is the scale length of the disk. Then the in-spiral timescale can be written in terms of the orbital timescale as:

$$\frac{T_{inspiral}}{\tau_{orb}} = \frac{\alpha M_*/M_c}{\ln(\alpha M_*/M_c)} \frac{X_{dm}^2}{\xi(X_{dm})} \frac{I_{dm}(p, R_{out}, R_{in})}{2\pi(R_{out}/pR_d)^2}, \quad (3.9)$$

where,

$$I_{dm}(p, R_{out}, R_{in}) = \int_{\frac{R_{out}}{pR_d}}^{\frac{R_{in}}{pR_d}} \frac{2+x^2}{3+x^2} \frac{x^2}{\sqrt{1+x^2}} dx. \quad (3.10)$$

The indefinite integral I_{dm} (above equation 3.10) can be written as $I_{dm} = I_{dm,1} + 3I_{dm,2}$ such that,

$$I_{dm,1} = \frac{1}{2}\left[x\sqrt{1+x^2} - 3\ln(x+\sqrt{1+x^2})\right], \quad (3.11)$$

and

$$I_{dm,2} = \frac{1}{2\sqrt{6}}\left[\ln(|\frac{2x}{\sqrt{1+x^2}} + \sqrt{6}|) - \ln(|\frac{2x}{\sqrt{1+x^2}} - \sqrt{6}|)\right] \quad (3.12)$$

We recall that in the above equations, R_d is the disk scale-length; X_{dm} and τ_{orb} (orbital timescale) are given by,

$$X_{dm}^2 \equiv \frac{V_{c0}^2}{V_0^2} = \frac{\alpha}{\alpha-1}h(R_{out}/pR_d), \quad and \quad \tau_{orb} = \frac{2\pi R_{out}^{3/2}}{\sqrt{G\alpha M_*}} \quad (3.13)$$

where V_{c0} is the circular velocity calculated at the location of the clump (R_{out}) due to the total dynamical mass ($M_{dyn} = \alpha M_*$) of the galaxy (circular velocity at the radius of the clump C3A (Fig. 2.4) is $V_{c0} = 25$ km s^{-1}). This, in turn, fixes the dark matter halo mass as $M_{dm} = (\alpha-1)M_*$; and $R_c = pR_d$. In all our calculations, we consider $p = 2$ case. Increasing the parameter p reduces the in-spiral timescale. Varying the parameter p either to 1 or 3 changes the in-spiral timescale by $\sim 10\%$. The function $h(y) = y^2/(1+y^2)$ represent the radial dependence of the circular velocity curve for the assumed dark matter

halo potential. The $T_{inspiral}$ for all the clumps detected in our sample of BCDs is given in Table 3.3.

3.2.2.1   Clump accretion rate and timescale:

Considering clump mass conservation, we estimate the net clump accretion rate in the galaxy as the sum of individual clump accretion rates due to the dynamical friction alone as

$$\dot{M}_{clump} = \sum_{j=1}^{n} \frac{M_{c,j}}{T_{inspiral,j}}, \tag{3.14}$$

where n denotes the total number of detected clumps in the galaxy; $T_{inspiral,j}$ denotes in-spiral time for j^{th} clump. We use this net clump accretion rate to find the time taken by the the clumps to reach the optical disk of the galaxy as:

$$\tau_{clump} = M_{clump}/\dot{M}_{clump} \tag{3.15}$$

where M_{clump} is the total clump mass. Additionally, we estimate the time taken by the clumps to transfer an amount of mass equal to the young stellar mass associated with the XUV disk (which is basically the FUV SFR in the XUV region integrated over a period of 100 Myr) into the optical region of the BCDs. We note here that galaxies with low ΔL_x, in the range of a few percent, have XUV disk masses that are less than the mass of all the clumps in the galaxy. The average radial profile could be flatter in the outer regions where we find the clumps, hence making it a Type III profile. To account for this in the timescale estimate of the outer disk evolution, we add the summed clump masses to the extrapolated XUV masses that come from the intrinsic fits; in those cases where ΔL_x is low. We do not include the clump masses in the XUV mass for the other cases. This difference in the two cases is evident in the FUV images also because the low-ΔL_x cases have outer clumps with much less contrast to the rest of the outer disk than the high-ΔL_x cases. We evaluate the timescales for XUV evolution as follows and present them in Table 3.3:

$$\tau_{XUV} = \frac{\Delta L_x M_{young}}{\dot{M}_{clump}} \quad ; \quad (\Delta L_x > 10\%) \tag{3.16}$$

$$\tau_{XUV} = \frac{\Delta L_x M_{young} + M_{clump}}{\dot{M}_{clump}} \quad ; \quad (\Delta L_x < 10\%) \tag{3.17}$$

where M_{young} is the FUV flux-derived stellar mass for the whole galaxy and ΔL_x is the FUV light fraction in the XUV region as described in equation 2.6.

3.2.2.2 Clump-clump collision timescale

There will be gravitational interaction among the clumps formed in the XUV disk that will result in their growth by merging together. This will increase their rate of infall to the central region of the host BCD. The clump infall time would then essentially be determined by the clump-clump collision timescale. The collision cross section of a clump (assuming spherical shape) is simply $\sigma_{clump} = \pi R_{clump}^2$, where R_{clump} is the radius of the clump. Then the mean free path of the clump is given by

$$l_{clump} = \frac{1}{n_{clump}\sigma_{clump}}, \tag{3.18}$$

where n_{clump} denotes the number density of the clumps within the XUV region. The clump-clump collision timescale, denoted as τ_{cc}, relative to the orbit time can then be written as

$$\frac{\tau_{cc}}{\tau_{orb}} = \frac{1}{2} \frac{M_{clump}}{\sum M_{clump}} \frac{H}{R_{out}} \left(\frac{R_{XUV}}{R_{clump}}\right)^2 \tag{3.19}$$

In the above, R_{XUV} is the size of the XUV region; H is the thickness of the disk and the rest of the parameters have their usual meaning. In all our calculations, we assume $H/R_{XUV} = 0.2$, for simplicity.

3.3   Results and Discussion

3.3.1   Clumpy disk star formation

We find massive FUV clumps in these BCDs. Of them, C3A is the brightest with 25.3 mag (others in Table 3.3). As such, these BCDs resemble star-forming disks of high-redshift massive galaxies[387]. We detect a total of 12 clumps: 4 with SExtractor, 2 with Noise Chisel, and 6 clumps by visual inspection of the XUV regions of the BCDs. The clumpy structure suggests unstable disks and that the clump size is comparable to the turbulent Jeans length. Thus strong torques may drive in-plane accretion. For GS3, the large FUV clumps have SFR of a few $\times 10^{-2}$ $M_\odot$ yr^{-1}. Considering timescales of ~ 100 Myr of the FUV emission, their masses would be a few $\times 10^6$ $M_\odot$ (Table 3.3). This is roughly 1% of the galaxy's total stellar mass, $M_* = 3.70 \times 10^8$ $M_\odot$ (Table 2.2). The stellar masses of the inner clumps in the HST optical image are similar, $\log M_*/M_\odot = 6.95$ and 6.33, which is based on their optical colours[388]. We reiterate that the photometry of faint objects will be influenced by the background. For example, in GS3, we obtain a local background of 28.77 mag arcsec^{-2} using *SExtractor*[21], as compared to a higher value of 28.53 mag arcsec^{-2} that is obtained as described in section 2.3.2. We check for this but do not find any drastic effect on the stellar mass estimates of the clumps. The mass of the fainter clump (C3B) differed by ~ 0.2 dex only. Similarly, varying the *SExtractor* parameters also brings changes in the clump mass estimates. For example, on changing the detection threshold from 1.5 to 2σ while keeping the smoothing kernel intact, the stellar mass of the clump C3A changes by ~ 0.2 dex. On the other hand, changing the smoothing kernel from gauss 1.5 to gauss 2.0 (at fixed detection threshold$=1.5\sigma$) has a lesser effect; e.g., clump mass of C3A changes by ~ 0.1 dex. Beyond a detection threshold >2 in SExtractor, most of the FUV clumps go undetected. Therefore, we finally use parameters (Table 3.1) motivated by those used in existing deep and large scale surveys[389, 390], especially to pick our faint FUV sources.
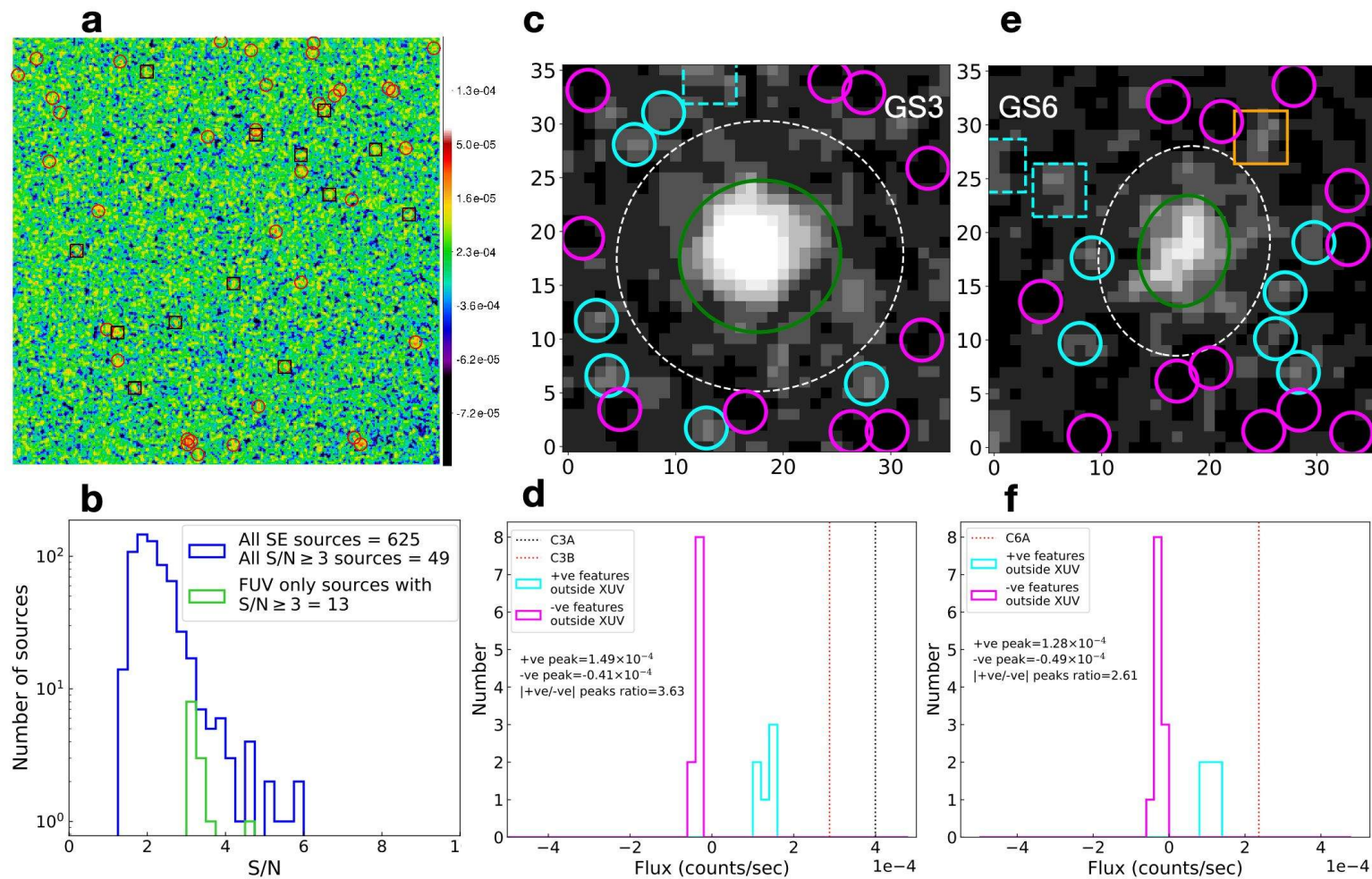
Figure 3.3: **Test for clump significance. a.** Patch of sky of size 341×341 pixels devoid of bright and large sources in the *GOODS-South* field. Red circles denote sources having S/N≥3 and their number is 49. Of these, 13 are marked with black circles that do not have any *HST* counterpart . **b.** S/N histogram of sources detected in the patch shown in **a**. Panel **c, e** GS3 and GS6 with the same size as presented in Fig.2.4 and 2.5. Cyan circles and boxes mark the SExtractor detected sources. Sources having S/N<3 are marked with cyan circles. Sources having S/N≥3 and *HST* counterparts are marked with cyan dashed squares. The orange square has S/N≥ 3 and no *HST* counterpart. Magenta circles mark noise dips below a flux value of zero. Panel **d, f** represent flux (measured within a fixed aperture of size 0.7" radius) histograms corresponding to panel **c, e.**[358]

3.3.2 Clump significance:

In what follows, we demonstrate the statistical significance of our FUV clumps. We choose a large patch (341x341 pixels = 20220 arcsec^2) of the *GOODS-South* image in the FUV and run *SExtractor* (and Noise Chisel) with the same settings that we used to find the clumps in our BCDs. This resulted in the detection of 625 (157) sources. Of these, 13 (11) FUV sources have S/N$\geq$3 and don't have any *HST* counterpart. This translates to a clump density of 0.0006429 (0.0005440) arcsec^{-2} in the patch. If these clumps would arise due to background fluctuations alone, we would expect ∼0.3 (0.2) similar clumps using SExtractor (and Noise Chisel) in the XUV regions per BCD. The combined area of the XUV region in the BCDs is ∼ 458.5 arcsec^2. We also randomly place elliptical apertures (same as red ellipses, shown in Fig. 3.1 and 3.2 on the same patch of the sky. This results in 0 out of 1604 apertures with S/N$\geq$3 and without any *HST* counterpart. To check our manual approach, we visually identify 435 FUV sources without *HST* counterparts in the same patch (after all *SExtractor* detected sources are removed) and estimate their S/N. We find that none of them have S/N$\geq$ 3. As an additional representative exercise, we present the S/N of the *SExtractor* detected sources outside the XUV regions, i.e. beyond the larger S/N=3 FUV boundaries of GS3 and GS6 in Table 3.2. We recall here that the XUV region is the region enclosed within

GS3			GS6		
x	y	S/N	x	y	S/N
-3.87	15.86	3.24 *	7.81	11.11	3.3 #
-13.55	-12.35	2.27	-17.33	8.64	3.2 *
-4.19	-16.88	2.60	-11.14	6.64	3.0 *
-10.45	9.46	2.30	12.57	1.91	2.4
11.17	-12.80	2.34	9.75	-3.00	2.3
-8.36	12.54	1.86	9.36	-6.63	2.3
-14.10	-7.29	2.25	11.48	-10.30	2.4
			-9.17	0.11	2.8
			8.80	8.26	2.1

Table 3.2: **S/N of *SExtractor* detected sources around GS3 and GS6.** The coordinate columns represent relative positions with respect to the galaxy's center. All the above tabulated sources are shown in Fig. 3.3 c,e with outlines. Those with * have S/N$\geq$3 with an *HST* counterpart and are marked with cyan boxes, and the one with # also has S/N$\geq$3 but has no *HST* counterpart and is marked with an orange box.

the S/N=3 extents of the galaxies in the optical and FUV band. These are highlighted in Fig. 3.3 c, e). We find that all 6 sources surrounding GS3 and 6 of the sources in GS6 have $S/N < 3$; we mark these with cyan circles in the figure. The cyan boxes (having *HST* counterparts) and orange box (without an *HST* counterpart) have $S/N > 3$. This implies that there isn't any detection with S/N>3 except those specified above, thereby supporting the detected FUV clumps in the galaxies. Additionally, we inspect the noise peaks (positive and negative) outside the galaxies within fixed apertures and compare their '*strengths*' with the actual detected clumps. We use fixed apertures of size equal to the FWHM of the FUV PSF. The positive peaks are the *SExtractor* detections specified above, while we use visual inspection to find the negative peaks. (see Fig. 3.3 c, e). Fig. 3.3 (d,f) shows the histograms of flux estimates mentioned above in the case of GS3 and GS6. The ratios of the positive peak flux to negative peak flux i.e., the peak-to-peak flux ratios are 3.6 and 2.6 for GS3 and GS6 respectively. These ratios are slightly on the higher side, possibly because the noise distribution in FUV (being dominated by low-photon statistics) is Poissonian rather than symmetric Gaussian. This exercise tells us that the flux values of the BCD clumps are larger than the fluctuations in the background.

The sensitivity of β to metallicity (Z), stellar ages and the SFH[391, 392] can introduce biases in the derived extinction. We use intrinsic SED models with $Z = Z_\odot$ and 0.4 $Z_\odot$, and find $\Delta\beta$ up to 0.26 or equivalently, $\Delta E(B-V)$ up to 0.06 mag only. At the same time, our clump stellar mass estimates are solely based on the assumption of a constant SFR for 100 Myr. We do not know the actual SFH of the clump star formation. To get an idea of the systematic uncertainty, we use STARBURST99 to model the clumps. For this, we try an instantaneous burst SFH that happened 100 Myr to 1 Gyr ago and a continuous star-formation history (CSFH) going on since the past 100 Myr to 200 Myr. We used a Salpeter IMF[370] (1-100 $M_\odot$), $E(B-V)$ value at $Z_\odot$ and a Calzetti [393] extinction curve. Then we compare the observed clump masses to the clump masses estimated from modelled FUV clumps. For an SFH with a 100 Myr old instantaneous burst, our mean clump mass is in good agreement with the mean modelled clump mass. Model masses (using model FUV fluxes)

gradually decrease by ~ 0.5 dex to 3.5 dex when burst age increases from 200 Myr to 1 Gyr. An increase of ~ 0.9 dex is seen for a 100 Myr old CSFH. We present the stellar mass estimates of the clumps in Table 3.3.

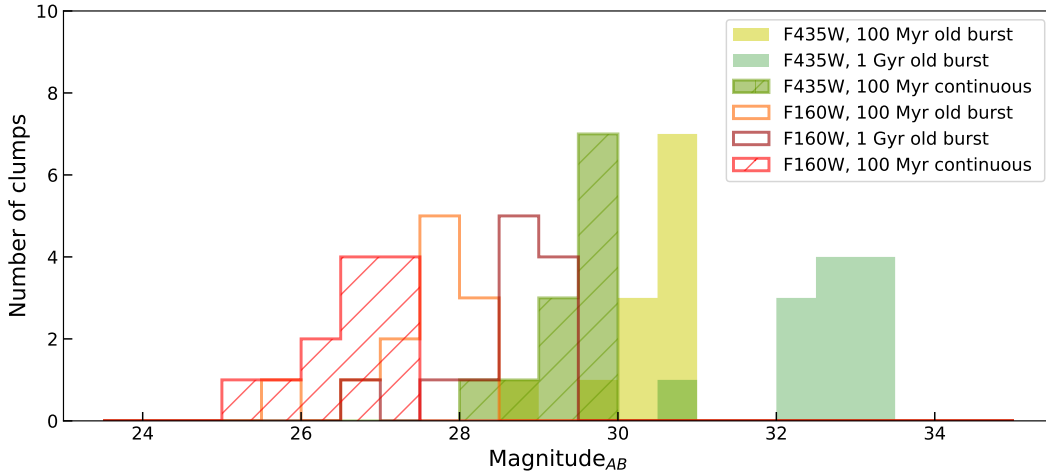*Figure 3.4:* **Expected optical-NIR magnitudes of FUV clumps in z~0.2 BCDs.**

We conduct an additional exercise using the above clump models to estimate the expected optical and NIR magnitudes with the HST. We find here that, the median apparent magnitude of the clumps with 100 Myr old burst of star formation would be ~ 30.6 mag and 27.7 mag in the F435W and F160W band respectively. For a 1 Gyr old burst, this would be 32.9 mag and 28.8 mag respectively. For a continuous star-formation activity that started 100 Myr ago, the apparent magnitude in the F435W band (and F160W) would be 29.6 mag (and 26.8 mag). It is important to note that the *GOODS-South* field has a varying depth over the whole field with the HST. As per Guo et al. 2013[394] and Whitaker et al. 2019[303], 5σ point-source limit for F435W filter can range from ~ 27.6 to 30.5 mag and that for F160W filter range from ~ 27.1 mag to 29.8 mag. It is important to note that the deepest regions are a small fraction of the total observed *GOODS-South* field. Our exercise suggests that the expected optical/NIR magnitudes of the FUV clumps detected in this work lie at or beyond the limits of current HST depths. However, there is an underlying assumption to this exercise that the initial size, mass and stellar density of the FUV clumps remain intact throughout the period we have considered here. But in reality, they may get dispersed or destroyed. Literature suggests that star formation history in galaxy outskirts is more likely to be bursty in nature[376]. If this is the case, the expected clump magnitudes in

the optical will be too faint (as revealed by this exercise) and they will not be detected. If the clumps were continuously forming stars over the past 100 Myr, they would have likely been detected by HST with its optical/NIR filters. We reiterate here that for this to happen, the clumps should also remain intact. However, we avoid any ambitious claims as we lack information on the nature of the gas present or other requisite details to better model the clumps in the outskirts of these galaxies. Nevertheless, if we make the assumption that the star formation in the galaxy outskirts is bursty[376], the optical counterparts of the clumps are expected to be too faint to be detected by the HST. We present the expected HST magnitude distribution of the clumps in Figure 3.4.

3.3.3 Clump accretion timescales

For GS3 with $M_* = 3.78 \times 10^8 M_\odot$, M_{dm}=6.42 $\times 10^8$ $M_\odot$, $\tau_{orb} = 1.7$ Gyr at $R_{out} = 7$ kpc. The Coulomb factor for GS3 $\ln \Lambda \simeq 5$. For the largest clump C3A in GS3, $T_{inspiral} \sim 5.6$ Gyr is 4.3 times the look-back time at z=0.1. For the clump in GS14 (z=0.1), C14A, $T_{inspiral} \sim 2.4$ Gyr. The clump mass divided by $T_{inspiral}$ gives the instantaneous clump accretion rate, and their sum for each galaxy gives the summed clump accretion rate, $\dot{M}_{clump}$. The average value of $\dot{M}_{clump}$ for all the galaxies is $\sim 1.1 \times 10^6$ $M_\odot$ Gyr^{-1}. For GS3, $\dot{M}_{clump} \sim 2.3 \times 10^6$ $M_\odot$ Gyr^{-1} and the average clump accretion time is $\tau_{clump} = 5.5$ Gyr. This time is less than Hubble time, implying that clump torques can lead to significant evolution of the outer structures. Moreover, due to differential shear in the outer disks, the clumps will come closer together and coalesce and form bigger clumps which will result in faster accretion. The clump collision time from the shear (τ_{cc} in Table 3.3) is approximately the orbit time. In GS3, the mean clump collision timescale is $\sim$1.5 Gyr which is close to its τ_{orb}. If these effects are taken into consideration, the clump accretion time could be shorter by a factor of 5 or more.

3.3.4 XUV disk accretion timescales

The mass of the young outer disk, i.e. the young XUV mass is larger than the total combined mass of the outer clumps in the BCDs. Hence, the clump torques are not sufficient to accrete all the mass in the young stellar disk

BCD	Clump ID	S/N	MAG mag	A_{FUV} mag	$SFRD_{clump}$ $M_\odot$ yr^{-1}kpc^{-2}	M_{clump} log $M_\odot$	$T_{insprial}$ Gyr	$\dot{M}_{clump}$ $M_\odot$ Gyr^{-1}	τ_{clump} Gyr	τ_{cc} Gyr	τ_{XUV} Gyr	τ_{SF} Gyr
GS1	†C1A	3.3	26.18	1.21	7.63×10^{-4}	6.42	12.6	0.21×10^6	12.5	0.9	14.6	1.7
GS2												1.8
GS3	$^{\#\dagger}$C3A	4.3 (4.8)	25.30	2.00	4.98×10^{-4}	6.84	5.6			1.0	6.6	3.4
	$^\#$C3B	3.7 (4.4)	25.46	2.00	4.82×10^{-4}	6.77	6.0	2.3×10^6	5.5	1.9		
GS4												8.1
GS5												11.9
GS6	*C6A	3.2	26.84	0.86	1.16×10^{-3}	6.49	7.5	0.43×10^6	7.2	1.5	31.3	2.5
GS7												1.1
GS10	*C10A	3.2	26.91	1.21	1.31×10^{-3}	6.50	8.3	0.40×10^6	7.9	1.8	54.9	1.7
GS11												0.8
GS12	$^{\#\dagger}$C12A	3.2 (3.6)	26.40	1.30	5.44×10^{-4}	5.90	11.8			1.1	26.3	4.2
	†C12B	3.4	26.53	1.30	6.90×10^{-4}	5.85	54.8			0.6		
	*C12C	4.0	26.28	1.30	9.42×10^{-4}	5.95	26.5			0.5		
	*C12D	3.2	26.67	1.30	1.30×10^{-4}	5.80	72.0	0.13×10^6	23.2	0.4		
GS13	*C13A	3.0	27.04	1.63	2.93×10^{-3}	6.76	18.6			0.9	26.6	1.6
	*C13B	3.4	26.64	1.63	7.89×10^{-3}	6.92	13.1	0.96×10^6	14.6	0.7		
GS14	$^{\#\dagger}$C14A	3.8 (3.0)	26.26	2.95	9.49×10^{-4}	6.83	2.4	3.0×10^6	2.2	1.8	3.7	7.7

Table 3.3: **Full FUV-clump analysis in our sample of BCDs. Column 1:** Clump IDs identified by *SExtractor* (#), Noise Chisel (†) and visual inspection (∗). **Column 2:** Measured S/N of the clumps (in *SExtractor* Kron-like apertures). **Column 3:** Clump magnitudes using *SExtractor* within Kron-like apertures (using detected pixel flux in the case of Noise Chisel and aperture fluxes in the case of visually identified clumps). **Column 4:** Internal dust extinction estimated using the UV-slope (β). **Column 5:** Clump star formation rate surface density. **Column 6:** Clump stellar mass. **Column 7:** Inspiral time of the clumps. **Column 8:** Net clump accretion rate. **Column 9:** Total clump accretion timescale. **Column 10:** Clump-clump collision timescale. **Column 11:** XUV disk evolution timescale. **Column 12:** Galaxy star formation time.

resulting in an XUV disk accretion time, $\tau_{XUV} > T_{inspiral}$. The XUV disk accretion time is several Hubble times for most of the BCDs (except for GS3: 6.6 Gyr and GS14: 3.7 Gyr; Table 3.3). At the same time, the accretion time for the additional outer disk old stars would be still longer. As such, we expect to observe extended disks of old stars in these systems. For example, in a recent work by Paswan et al. 2022[395] we find a nearby BB that hosts an underlying extended old LSB disk. With JWST now, we expect to be able to look for such extended old stellar disks and understand their contribution to overall disk mass assembly. Interestingly, $T_{inspiral}$ is comparable to the galactic star formation time for our BCDs, $\tau_{SF} = M_{*,total}/SFR$ (Table 3.3). These timescales are shorter than Hubble time and for most of them, these are comparable to their lookback times as well. Therefore, the relatively short $\tau_{SF} \sim$ few Gyr - implies a rapid buildup of the main disk at the same time as the outer disk clumps move inward. For shorter clump accretion times by a factor of 5 or more due to clump collision, the effective accretion time for the young stellar mass in the XUV disk of BCDs with $\Delta L_x \geq 10\%$, $\tau_{XUV} \sim$ a few Gyr. In GS3 and GS14 with this revision, $\tau_{XUV} \sim 1$ Gyr. Such high accretion rates will likely be accompanied by simultaneous gas accretion.

The estimated accretion times should be considered as upper limits because the presence of gas will make the young clumps even more massive. Since typical star-formation efficiencies in the youngest regions are only a few percent[30], these clumps would contain a lot of unused gas; if taken into account, it would increase the clump masses by a factor of 50 or so. This will decrease the timescale in inverse proportion. The disk stars and gas may also exert torques on a clump [383] as a result of which the timescale would be smaller than just from the halo torques.

3.4 Summary and Conclusions

In this Chapter, we present the study of the massive FUV clumps in the outer parts of distant BCDs hosting XUV disks. The outer as well as inner clumpy morphology, as revealed by *HST* observations, indicate gravitationally unstable disks. The FUV clumps do not contain *HST* counterparts which

is indicative of recently formed stars within the past 100 Myrs. We perform a careful and robust identification of the FUV-only clumps using automated tools as well as manual inspection so as to avoid artifacts. We find that the identified clumps having S/N $\geq$ 3 have a low probability of being noise peaks. These clumps are of the order of a few $\sim10^6$ M$_\odot$ which is about 1% of their total stellar masses. Such massive clumps in a gravitationally unstable disk will experience dynamical friction leading to their inward radial migration. In a dark matter halo only set-up, we estimate the time that will be taken by these massive outer clumps to move inwards. We find that on average the accretion rate is $\sim10^6$ M$_\odot$Gyr^{-1}. The clumps can also come closer and combine due to differential shear in the galactic disk. We find that this will happen over $\sim$orbital timescales of the clumps leading to faster infall of the even larger clumps. The clumps therefore produce enough torques to drive them, or an equivalent mass, inward to the optical disk, building a more centrally concentrated structure. These torques are not large enough to bring in the whole outer disks, which should likely fade away into the extended old disks[27] and halos[396] of today's BCDs[397]. Such a scenario may explain a similar evolutionary history in other compact starbursts as well.